Another one grinds the dust: variability of the planetary debris disc at the white dwarf SDSS J104341.53+085558.2

Christopher J. Manser,[1][*] Boris T. Gänsicke,[1] Detlev Koester,[2] Thomas R. Marsh[1] and John Southworth[3]

[1]*Department of Physics, University of Warwick, Coventry CV4 7AL, UK*
[2]*Institut für Theoretische Physik und Astrophysik, University of Kiel, D-24098 Kiel, Germany*
[3]*Astrophysics Group, Keele University, Staffordshire ST5 5BG, UK*

ABSTRACT

We report 9 yr of optical spectroscopy of the metal-polluted white dwarf SDSS J104341.53+085558.2, which presents morphological variations of the line profiles of the 8600 Å Ca II triplet emission from the gaseous component of its debris disc. Similar changes in the shape of the Ca II triplet have also been observed in two other systems that host a gaseous disc, and are likely related to the same mechanism. We report the Mg, Si, and Ca abundances of the debris detected in the photosphere of SDSS J1043+0855, place upper limits on O and Fe, and derive an accretion rate of $(2.5–12) \times 10^8$ g s^{-1}, consistent with those found in other systems with detected debris discs. The Mg/Si ratio and the upper limit on the Fe/Si ratio of the accreted material broadly agree with those found for the crust of the Earth. We also review the range of variability observed among white dwarfs with planetary debris discs.

Key words: accretion, accretion discs – line: profiles – circumstellar matter – stars: individual: SDSS J104341.53+085558.2230 – white dwarfs.

1 INTRODUCTION

The detection of metal pollution in white dwarf atmospheres provides strong evidence that 25–50 per cent of white dwarfs host remnants of planetary systems (Zuckerman et al. 2003; Koester, Gänsicke & Farihi 2014; Koester & Kepler 2015). The survival of planets through the post-main-sequence evolution of their host star is further supported by the detection of more than 35 dusty debris discs at white dwarfs with metal pollution (Kilic et al. 2006; Farihi, Zuckerman & Becklin 2008; Farihi, Jura & Zuckerman 2009; Jura, Farihi & Zuckerman 2009; Debes et al. 2011; Hoard et al. 2013; Bergfors et al. 2014; Rocchetto et al. 2015), and is also predicted by theoretical studies (Villaver & Livio 2007; Veras & Gänsicke 2015).

Debris discs around white dwarfs are thought to be produced by the tidal disruption of asteroids (or comets) scattered on to a highly eccentric orbit by planets in the system (Graham et al. 1990; Jura 2003). While recent simulations have begun to explore the formation and evolution of these discs; from the initial disruption of the planetesimal and the shrinking of its orbit (Debes, Walsh & Stark 2012; Veras et al. 2014, 2015), to the dynamics and interactions of the debris within the disc (Rafikov 2011; Metzger, Rafikov & Bochkarev 2012), many aspects remain poorly understood.

Over the last decade, gaseous debris discs have been detected around eight white dwarfs, all of which also host circumstellar dust and have metal-polluted photospheres (Gänsicke et al. 2006, 2008; Gänsicke, Marsh & Southworth 2007; Gänsicke 2011; Farihi et al. 2012; Melis et al. 2012; Wilson et al. 2014; Guo et al. 2015). These systems were identified by the detection of Ca II 8498.02 Å, 8542.09 Å, 8662.14 Å emission lines (henceforth the Ca II triplet, air wavelengths are given).

So far only four of these eight gas disc systems have multi-epoch spectroscopy over time-scales of years, three of which show variability in the Ca II emission of the gaseous disc; either as significant changes in the morphology of the Ca II triplet (Wilson et al. 2015; Manser et al. 2016), or as a decrease in strength of the lines (Wilson et al. 2014). It is thought that the gaseous components of the debris discs in these systems are tracers of dynamic activity (Gänsicke et al. 2008; Wilson et al. 2014, 2015; Manser et al. 2016).

The gaseous disc around SDSS J104341.53+085558.2 (henceforth SDSS J1043+0855) was discovered by Gänsicke et al. (2007) via the detection of Ca II triplet emission. An infrared excess was detected by Melis et al. (2010) and Brinkworth et al. (2012), confirming the presence of a dusty disc in SDSS J1043+0855. Here, we report 9 yr of spectroscopic observations of SDSS J1043+0855 that reveal a change in the morphology of the Ca II triplet, similar to those seen in other gaseous disc systems (SDSS J122859.93+104032.9 and SDSS J084539.17+225728.0, henceforth SDSS J1228+1040 and SDSS J0845+2257, Wilson et al. 2015; Manser et al. 2016).

[*] E-mail: C.Manser@warwick.ac.uk

Table 1. Log of observations of SDSS J1043+0855.

Date	Telescope/instrument	Wavelength range [Å]	Resolution [Å]	Exposure time [s][a]
2003 April 05	SDSS	3800–9200	2.9	2900
2007 February 03	*WHT*/ISIS	7400–9200	2.0	4800
2009 February 16	*WHT*/ISIS	6000–8900	3.7	3950
2010 April 22	*WHT*/ISIS	8100–8850	1.1	7200
2011 January 29	VLT/X-Shooter	2990–10400	1.12	2950/2840
2011 May 30	VLT/X-Shooter	2990–10400	1.15	2950/2840
2012 January 03	SDSS	3602–10353	3.2	2702

Note. [a]Different exposure times for the individual X-Shooter arms (UVB/VIS). We did not use data collected by the NIR arm of X-Shooter as the signal-to-noise ratio was too poor.
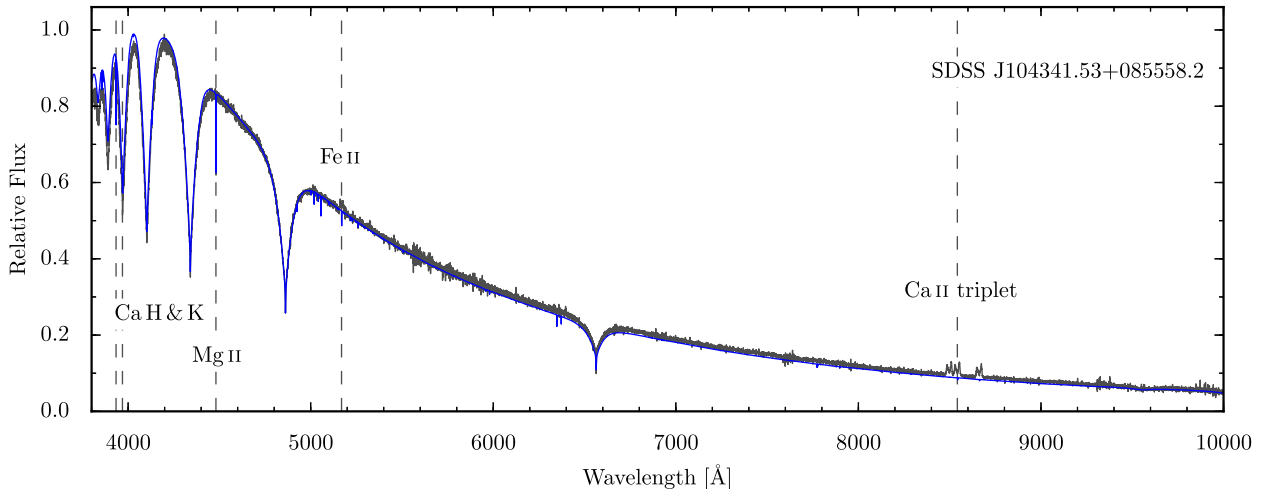

Figure 1. X-Shooter spectra of SDSS J1043+0855 (grey, obtained in 2011 January and May) together with a model atmosphere fit (blue) using the atmospheric parameters listed in Table 2. The strongest emission and absorption lines have been labelled (note that the Fe II feature is in emission).

We also present the accretion rates of the debris on to the white dwarf and the metal abundances of the debris.

2 OBSERVATIONS

We obtained optical spectroscopy of SDSS J1043+0855 from 2003 to 2012 with several instruments: X-Shooter (Vernet et al. 2011) on the ESO Very Large Telescope (VLT); the 2.5 m Sloan Digital Sky Survey telescope (SDSS, data retrieved from DR7 and DR9, Gunn et al. 2006; Abazajian et al. 2009; Eisenstein et al. 2011; Smee et al. 2013; Ahn et al. 2014); and the Intermediate dispersion Spectrograph and Imaging System (ISIS) on the *William Herschel Telescope* (*WHT*). A log of the observations is summarized in Table 1. The X-Shooter data were reduced within the REFLEX[1] reduction work flow using the standard settings and optimizing the slit integration limits (Freudling et al. 2013). The sky spectrum of each observation was used to determine the spectral resolution. The first ISIS spectrum of SDSS J1043+0855 was reported in Gänsicke et al. (2007), the additional ISIS spectra were obtained with a similar setup, and were reduced in the same fashion (see Farihi et al. 2012 and Wilson et al. 2014 for additional details). We removed the telluric lines present in the VIS arm of the X-Shooter spectra using the X-Shooter Spectral Library (XSL) provided by Chen et al. (2014), and applying the method outlined in Manser et al. (2016) (see Fig. 1 for an example).

---

[1] Documentation and software for REFLEX can be obtained from http://www.eso.org/sci/software/reflex/.

3 EVOLUTION OF THE CALCIUM EMISSION PROFILE

3.1 Double-peaked emission from a disc

The characteristic emission profile from a gaseous disc with a radially symmetric intensity distribution and circular orbit is a symmetric, double-peaked emission profile (see fig. 1 of Horne & Marsh 1986). The width of the profile arises from the wide range of velocities projected along the line of sight and can reveal details about the structure and geometry of the gaseous disc. The largest velocities correspond to material at the inner disc radius, which can hence be determined from the full width at zero intensity, i.e. the point at which the emission drops to the continuum level, and with knowledge of the inclination, i, using $R \sin^2 i = R_{obs}$, where R and R_{obs} denote the actual and observed radii, respectively. We define the maximum redshifted/blueshifted velocities to represent the red/blue inner edges of the disc. The outer radius can be estimated from the peak separation in the double-peaked profile.

Any departure from a radially symmetric, circular disc will manifest itself as asymmetries in the double-peaked emission profile. An eccentric disc of uniform intensity, for example, would generate an asymmetric double-peaked profile if viewed along the semi-minor axis, as there is an asymmetry in the velocity distribution of the material, as well as in the total red and blueshifted light emitted from the disc. We use this insight below to discuss the changes in the line profiles observed at SDSS J1043+0855.
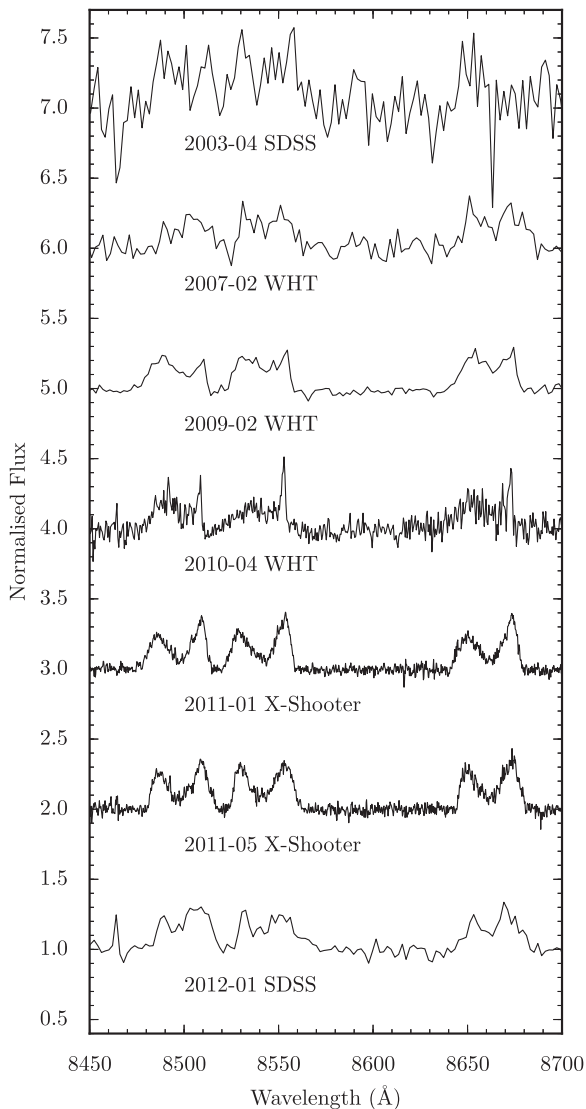
Figure 2. Time series spectroscopy of the Ca II triplet of SDSS J1043+0855 spanning 9 yr. The spectra are normalized and offset in steps of one from the 2012 January observation.

3.2 Variation of the calcium emission lines

The Ca II triplet in SDSS J1043+0855 changes in morphology over a time-scale of 9 yr (Fig. 2). All three components of the triplet vary in the same manner and are henceforth referred to in singular.

The initial three spectra are noisy and of low resolution, showing a broad line profile. In contrast, finer features appear in the higher resolution 2010 *WHT* spectrum, namely a sharp redshifted peak and a gradual drop off to blueward wavelengths, revealing a clear asymmetry in the red and blue inner edges of the disc. This asymmetry decreases in the 2011 January spectrum, and vanishes in the 2011 May spectrum. The second SDSS spectrum obtained in 2012 shows no sign of any sharp departures from symmetry, although it is of relatively low spectral resolution. In Section 5 we discuss the similarities, and the possible origin, of the observed variations with those seen in other systems.

3.3 Inclination of the disc

In the 2011 January and May spectra, the 'valley' in between the two peaks of the emission profiles almost reaches the continuum
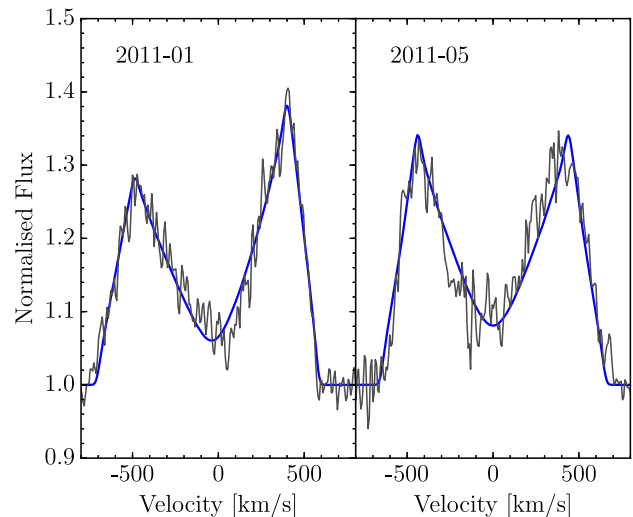

Figure 3. Model fit to the normalized 8542.09 Å component of the Ca II triplet for the 2011 January and May X-shooter spectra, from which we obtain an inclination of $i \simeq 74°$ for the disc at SDSS J1043+0855. The model applies the formulation described in Horne & Marsh (1986) which has been expanded to include eccentric orbits (see Appendix A for more details).

level, which suggests that the debris disc is optically thick and seen at a large inclination. Horne & Marsh (1986) have shown that in an optically thick accretion disc, line emission is more likely to escape along paths of largest velocity gradient provided by Keplerian shear flow, which is at a minimum for purely tangential or radial emission through the disc. For an observer looking through the disc at an inclination of 90° (edge on), material travelling perpendicular to the line of sight (emission in the 'valley') will be emitting along the radial direction of the disc and will therefore be suppressed.

While the formulation described in Horne & Marsh (1986) was developed for circular orbits, it was expanded to include eccentric orbits in order to model the emission profile of SDSS J1228+1040 obtained in 2006 (Gänsicke et al. 2006), and we give additional details on this extension in Appendix A. We fit the emission profiles of the 2011 January and May spectra of SDSS J1043+0855 in the same manner (see Fig. 3), and obtain an inclination of $i \simeq 76°$ and 72°, respectively, leading to an average inclination of $i = 74°$. The statistical uncertainty obtained for the two inclinations was $\pm 0°.5$, which is probably an underestimate, and a more realistic uncertainty is taken to be $\simeq \pm 5°$.

4 METAL ABUNDANCES IN THE PHOTOSPHERE OF SDSS J1043+0855

We fitted the two SDSS spectra with DA (hydrogen dominated) white dwarf model atmospheres using the methods described in Gänsicke et al. (2012) and Koester et al. (2014), and find $T_{\mathrm{eff}} = 17879 \pm 195$ K, and $\log g = 8.124 \pm 0.033$, corresponding to $M_{\mathrm{WD}} = 0.693 \pm 0.020 \, \mathrm{M_\odot}$ and $R_{\mathrm{WD}} = 0.0120 \pm 0.0003 \, \mathrm{R_\odot}$ (see Table 2). Using the initial-to-final mass relation of Casewell et al. (2009), Kalirai et al. (2008), Catalán et al. (2008), and Williams, Bolte & Koester (2009), we estimate the mass of the white dwarf progenitor to be $2.76 \pm 0.04 \, \mathrm{M_\odot}$.

We note that while the atmospheric parameters derived here are consistent with previous measurements (Eisenstein et al. 2006; Gänsicke et al. 2007; Tremblay, Bergeron & Gianninas 2011; Kleinman et al. 2013) the *ugriz* photometry suggests a lower effective

Table 2. Metal-polluted white dwarfs with circumstellar gas detected in emission (e) or absorption (a), and evidence for photometric or spectroscopic variability (v). System parameters and accretion rates are given with errors where known. Values derived or updated in this paper are set in italics. [1]Dufour et al. (2012), [2]Wilson et al. (2015), [3]Farihi et al. (2012), [4]Xu & Jura (2014), [5]Gänsicke et al. (2007), [6]Melis et al. (2010), [7]This paper, [8]Guo et al. (2015), [9]Gänsicke et al. (2006), [10]Gänsicke et al. (2012), [11]Koester et al. (2014), [12]Manser et al. (2016), [13]Koester et al. (2005), [14]Voss et al. (2007), [15]Melis et al. (2012), [16]Wilson et al. (2014), [17]Vennes & Kawka (2013), [18]Koester & Wilken (2006), [19]Debes et al. (2012), [20]Vanderburg et al. (2015), [21]Xu et al. (2016).

Name	Type	log g (g cm^{-2})	$T_{\rm eff}$ (K)	$M_{\rm WD}$ (M$_{\odot}$)	$\tau_{\rm cool}$ (Myr)	$\dot{M}$ ($\times 10^8$ g s^{-1})	Features	Ref
SDSS J0738+1835	DB	8.4 (0.2)	13950 (100)	0.841 (0.131)	477 (160)	1300	e	1
SDSS J0845+2257	DB	8.18 (0.20)	19780 (250)	*0.73 (0.11)*	*122 (44)*	160	e, v	2
SDSS J0959−0200	DA	8.06 (0.03)	13280 (20)	0.64 (0.02)	*324 (17)*	0.32	e, v	3, 4
SDSS J1043+0855	DA	*8*	*17879 (195)*	*0.693 (0.020)*	*153 (10)*	*(2.5–12)*	e, v	5, 6, 7
WD 1144+0529	DA	7.74 (0.03)	23027 (219)	0.49 (0.03)	21.2 (1.9)	−	e	8
SDSS J1228+1040	DA	8.150 (0.089)	20713 (281)	0.705 (0.051)	100 (5)	5.6	e, a, v	6, 9, 10, 11, 12
HE 1349−2305	DA	8.133	18173	0.673	149.4	1.3	e	13, 14, 15
SDSS J1617+1620	DA	8.11 (0.08)	13520 (200)	0.68 (0.05)	350 (50)	(6.4–7.8)	e, v	16
PG 0843+516	DA	7.902 (0.089)	22412 (304)	0.577 (0.047)	*42 (4)*	10.2	a	11
WD 1054−226	DA	8.04 (0.03)	7903 (16)	−	*1255 (92)*	−	a	17
WD 1124−293	DA	8.1	9700	0.66	*843*	1.3	a	18, 19
WD 1145+017	DB	−	15900 (500)	−	175 (75)	430	a, v	20, 21

temperature, even when allowing for the maximum reddening along the line of sight obtained from Schlafly & Finkbeiner (2011). This discrepancy is likely due to a higher amount of extinction, either by a denser patch in the interstellar medium that remains unresolved in the dust maps, or by circumstellar dust. We speculate that there could be additional dust in the system, which may not be associated with the dusty component of the debris disc at SDSS J1043+0855 (Melis et al. 2010; Brinkworth et al. 2012), and could possibly be the cause of the observed reddening.

Using the system parameters, the metal absorption lines detected in the spectra of SDSS J1043+0855 were modelled (see Fig. 4) to measure abundances relative to hydrogen which are given in Table 3, along with the diffusion time-scales and accretion fluxes. The abundance by number of Mg, Ca, and an upper limit for Fe relative to Si were found to be log (Mg/Si) = -0.64 ± 0.21, log (Ca/Si) = -1.33 ± 0.24, and log (Fe/Si) ≤ 0.19. From fig. 7 of Jura & Young (2014), the ratios of Mg and Fe to Si are broadly consistent with those found for the crust of the Earth, and imply the accreted object is processed rather than having a 'chondritic' composition (Zuckerman et al. 2007; Xu et al. 2013, 2014). This is also supported by the relatively low number abundance of Mg with respect to Ca, log (Mg/Ca) = 0.70 ± 0.25, when compared to a sample of 60 externally polluted white dwarfs (see fig. 1 of Jura & Xu 2013). Similarly low log (Mg/Ca) ratios have also observed at other white dwarfs that are thought to accrete crust material, such as NLTT 43806 and NLTT 19868 (Zuckerman et al. 2011; Kawka & Vennes 2016).

We also note that the Ca K 3934 Å feature shows clear emission in the averaged, normalized X-Shooter spectra (Fig. 4). Similar emission is seen at SDSS J1228+1040, which also revealed a difference in morphology between the Ca H and K profiles and the Ca II triplet, although the signal-to-noise of the current SDSS 1043+0855 spectra is not high enough to determine this (Manser et al. 2016).

We estimate the total accretion rate for each element from the mass flow rates given in Table 3, assuming a bulk Earth composition and the respective mass fractions of each element (from Allègre et al. 2001). The resulting range from Mg, Si, and Ca, $\dot{M}_{\rm Total} = 2.5 \times 10^8 - 1.2 \times 10^9$ g s^{-1}, reflects the uncertainty in the bulk abundances of the planetary debris, but agrees well with the distribution of accretion rates inferred for 19 other metal-polluted DA white dwarfs
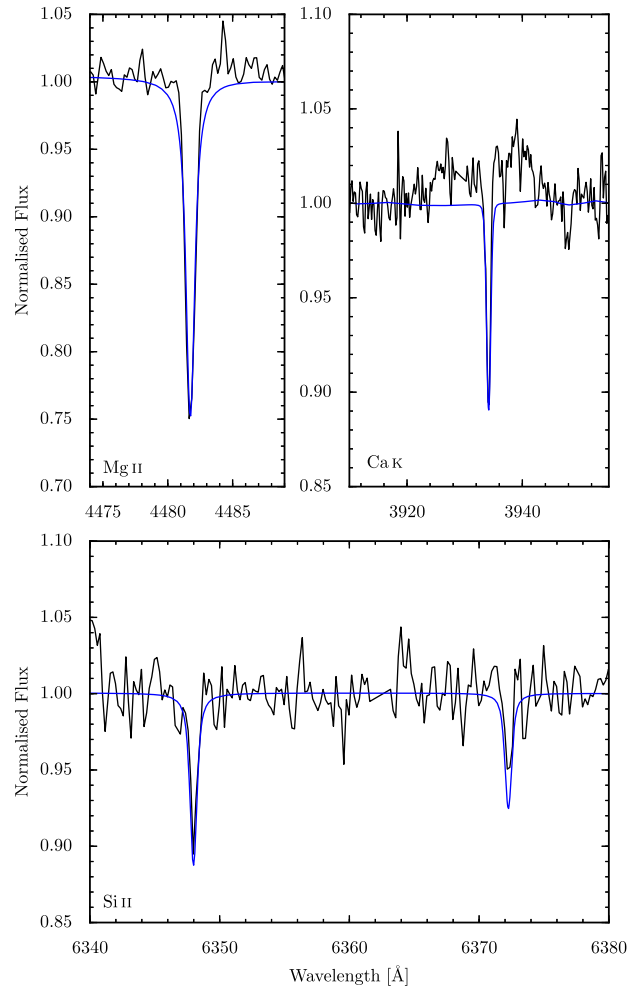

Figure 4. Model fits (blue) to absorption lines present in the combined X-Shooter spectra of SDSS J1043+0855 (black). The Ca K feature also contains a clearly detected emission profile from the gaseous disc.

Table 3. Diffusion time-scales, τ_{diff}, and average accretion fluxes, $\dot{M}$, for the metals detected in the photosphere of SDSS J1043+0855. Photospheric abundances by number are given with respect to hydrogen.

Element	log [Z/H]	τ_{diff} [h]	$\dot{M}$ [g s^{-1}]	Bulk Earth mass fraction [%]^a	Inferred total $\dot{M}$ [g s^{-1}]
8 O	<-4.00	65.0	$<2.0 \times 10^9$	32.4	$<6.2 \times 10^9$
12 Mg	$-5.15\ (0.15)$	26.5	4.0×10^7	15.8	2.5×10^8
14 Si	$-4.80\ (0.15)$	13.8	2.0×10^8	17.1	1.2×10^9
20 Ca	$-6.00\ (0.20)$	18.6	1.3×10^7	1.6	8.0×10^8
26 Fe	<-4.70	11.1	$<6.3 \times 10^8$	28.8	$<2.2 \times 10^9$

Note. ^{a}We infer a total accretion rate based on the mass fluxes assuming a bulk Earth composition and the respective mass fractions for each element (from Allègre, Manhès & Lewin 2001).

with dusty discs (Bergfors et al. 2014). For reference, the total accretion rate of SDSS J1228+1040 (where accretion fluxes for all major elements were measured from *HST*/COS ultraviolet spectra) is 5.6×10^8 g s^{-1} (Gänsicke et al. 2012).

5 DISCUSSION

Up until the last decade, debris discs around white dwarfs have appeared static in nature, with no significant detections of variability in the properties of the disc itself or in the strength of the absorption lines in metal-polluted systems. Due to the short diffusion time-scales at the majority of these systems (Koester et al. 2014), any change in the strength of the absorption lines would imply a change in the accretion rate on to the white dwarf. von Hippel & Thompson (2007) claimed changes in the equivalent width of the photospheric Ca II K line over a time-scale of days at GD 29–38, however additional observations obtained by Debes & López-Morales (2008) did not confirm such variation, and they concluded further data were required to determine the possible variable nature of the accretion on to the white dwarf.

In recent years, the spectroscopic monitoring of gaseous discs has revealed variability that gives us insight into their formation and dynamics. Table 2 lists the stellar parameters of the eight published gas disc systems. Other than SDSS J1043+0855, there are four gaseous disc systems with multi-epoch spectroscopy: SDSS J161717.04+162022.4 (Wilson et al. 2014, henceforth SDSS J1617+1620), SDSS J0845+2257 (Gänsicke et al. 2008; Wilson et al. 2015), SDSS J1228+1040 (Manser et al. 2016), and SDSS J073842.56+183509.6 (Gänsicke 2011; Dufour et al. 2012, henceforth SDSS J0738+1835).

SDSS J0845+2257, SDSS J1228+1040, and SDSS J1617+1620 all show variations on a time-scale of years, but follow two distinct types of evolution. In SDSS J1617+1620 the Ca II triplet emission gradually decreased in strength over a time-scale of eight years while not undergoing noticeable changes in the line profile shape (Wilson et al. 2014). In contrast, the changes seen in SDSS J0845+2257 and SDSS J1228+1040 are of a morphological nature, analogous to the changes we present here for SDSS J1043+0855. Table 4 lists the equivalent widths (subject to systematic uncertainties related to the method used in continuum fitting, as well as the statistical uncertainties given in Table 4) of the Ca II emission lines in SDSS J1043+0855, which do not show any long-term decay of the equivalent width of the Ca II triplet such as seen at SDSS J1617+1620. Only SDSS J0738+1835 has displayed no changes in the shape and strength of the Ca II triplet over a period of 6 yr, although only three epochs are available, with two of them spaced only a year apart.

Manser et al. (2016) showed that the variable Ca II triplet line profiles of SDSS J1228+1040 could be interpreted as the emis-

Table 4. Equivalent width measurements of the Ca II triplet in SDSS J1043+0855. The errors given here are purely statistical.

Date	Equivalent width [Å]
2003–04	-27 (3)
2007–02	-22 (1)
2009–02	-15 (1)
2010–04	-13 (1)
2011–01	-18 (1)
2011–05	-20 (1)
2012–01	-19 (1)

sion from a fixed intensity pattern that precesses over a time-scale of decades, possibly indicating a young debris disc that still has eccentric orbits and has not fully circularised. General relativistic precession will cause the debris to precess with a radially dependent period, causing orbits to cross one another and inducing collisions which produces the observed gaseous component to the debris disc.

While the evolution of the emission from SDSS J1043+0855 appears to be remarkably similar to SDSS J1228+1040 and SDSS J0845+2257, the data have a lower signal to noise and have fewer epochs, and thus, while it is likely that the same physical mechanism is responsible for the evolution of the line profiles observed in all three systems, regular spectroscopic monitoring of all gas discs is necessary to develop a more detailed understanding of the dynamical processes present in planetary debris discs around white dwarfs.

Variability of debris discs is not only limited to the Ca II triplet line profile. The dusty disc around SDSS J0959−0200 was observed to significantly decrease in infrared flux by Xu & Jura (2014), who propose two mechanisms by which the disc could be depleted; a recent planetesimal impact on the disc, or instability near the inner edge. We suggest an additional scenario of a vertically extended cloud of dust, generated from an asteroid colliding with a pre-existing disc (Jura 2008). Such an optically thin cloud would temporarily add to the infrared emission of the optically thick disc, but the overall infrared emission from the system would decrease as the dust cloud settled into the disc.

In Table 2 we also include four additional systems where circumstellar absorption of gaseous material has been detected around the host white dwarf, including WD 1145+017, which is orbited by highly dynamic debris, transiting the white dwarf with periods of $\simeq4.5$ h (Vanderburg et al. 2015; Gänsicke et al. 2016; Rappaport et al. 2016; Xu et al. 2016). WD 1145+017 is unequivocally a highly dynamical and evolving system with a planetesimal currently undergoing disruption, and also hosts circumstellar gas absorption (Xu et al. 2016). Curiously, the detection of absorption due to circumstellar gas does not correlate with the presence of

Ca ɪɪ triplet emission: SDSS 1228+1040 is so far the only system in which both have been detected (Gänsicke et al. 2012). We note that circumstellar gas has been detected also around a number of hot and young white dwarfs, their origin is probably diverse in nature and not unambiguously associated with evolved planetary systems (Dickinson et al. 2012; Barstow et al. 2014).

6 CONCLUSIONS

We report here the morphological variability of the Ca ɪɪ triplet in SDSS J1043+0855 on a time-scale of 9 yr. The evolution of the Ca ɪɪ triplet reported here is similar to that of two other systems, SDSS J1228+1040 and SDSS J0845+2257.

We have also analysed the optical spectra of SDSS J1043+0855 to determine its stellar parameters and the photospheric metal abundance. The Mg/Si and (upper limit to the) Fe/Si ratios of the planetary debris that has been accreted on to the white dwarf are broadly consistent with those of the crust of the Earth.

The recent detection of the 'real time' disruption of a planetesimal at WD 1145+017, along with the dynamical evolution seen at the gaseous discs SDSS J1043+0855, SDSS J1228+1040, SDSS J1617+1620, and SDSS J0845+2257 reveals that variability at planetary systems around white dwarfs is more common than was initially thought. Additional spectroscopic and photometric monitoring of all the gaseous discs known so far is key to developing a more detailed understanding of the dynamical processes present in planetary debris discs at white dwarfs.

REFERENCES

Abazajian K. N. et al., 2009, ApJS, 182, 543
Ahn C. P. et al., 2014, ApJ, 211, 17
Allègre C., Manhès G., Lewin E., 2001, Earth Planet. Sci. Lett., 185, 49
Barstow M. A., Barstow J. K., Casewell S. L., Holberg J. B., Hubeny I., 2014, MNRAS, 440, 1607
Bergfors C., Farihi J., Dufour P., Rocchetto M., 2014, MNRAS, 444, 2147
Brinkworth C. S., Gänsicke B. T., Girven J. M., Hoard D. W., Marsh T. R., Parsons S. G., Koester D., 2012, ApJ, 750, 86
Casewell S. L., Dobbie P. D., Napiwotzki R., Burleigh M. R., Barstow M. A., Jameson R. F., 2009, MNRAS, 395, 1795
Catalán S., Isern J., García-Berro E., Ribas I., Allende Prieto C., Bonanos A. Z., 2008, A&A, 477, 213

Chen Y.-P., Trager S. C., Peletier R. F., Lançon A., Vazdekis A., Prugniel P., Silva D. R., Gonneau A., 2014, A&A, 565, A117
Debes J. H., López-Morales M., 2008, ApJ, 677, L43
Debes J. H., Hoard D. W., Wachter S., Leisawitz D. T., Cohen M., 2011, ApJS, 197, 38
Debes J. H., Walsh K. J., Stark C., 2012, ApJ, 747, 148
Dickinson N. J., Barstow M. A., Welsh B. Y., Burleigh M., Farihi J., Redfield S., Unglaub K., 2012, MNRAS, 423, 1397
Dufour P., Kilic M., Fontaine G., Bergeron P., Melis C., Bochanski J., 2012, ApJ, 749, 6
Eisenstein D. J. et al., 2006, ApJS, 167, 40
Eisenstein D. J. et al., 2011, AJ, 142, 72
Farihi J., Zuckerman B., Becklin E. E., 2008, ApJ, 674, 431
Farihi J., Jura M., Zuckerman B., 2009, ApJ, 694, 805
Farihi J., Gänsicke B. T., Steele P. R., Girven J., Burleigh M. R., Breedt E., Koester D., 2012, MNRAS, 421, 1635
Freudling W., Romaniello M., Bramich D. M., Ballester P., Forchi V., García-Dabló C. E., Moehler S., Neeser M. J., 2013, A&A, 559, A96
Gänsicke B. T., 2011, in Schuh S., Drechsel H., Heber U., eds, in AIP Conf. Ser. Vol. 1331, Planetary Systems Beyond the Main Sequence. Am. Inst. Phys., New York, p. 211
Gänsicke B. T., Marsh T. R., Southworth J., Rebassa-Mansergas A., 2006, Science, 314, 1908
Gänsicke B. T., Marsh T. R., Southworth J., 2007, MNRAS, 380, L35
Gänsicke B. T., Koester D., Marsh T. R., Rebassa-Mansergas A., Southworth J., 2008, MNRAS, 391, L103
Gänsicke B. T., Koester D., Farihi J., Girven J., Parsons S. G., Breedt E., 2012, MNRAS, 424, 333
Gänsicke B. T. et al., 2016, ApJ, 818, L7
Graham J. R., Matthews K., Neugebauer G., Soifer B. T., 1990, ApJ, 357, 216
Gunn J. E. et al., 2006, AJ, 131, 2332
Guo J., Tziamtzis A., Wang Z., Liu J., Zhao J., Wang S., 2015, ApJ, 810, L17
Hoard D. W., Debes J. H., Wachter S., Leisawitz D. T., Cohen M., 2013, ApJ, 770, 21
Horne K., Marsh T. R., 1986, MNRAS, 218, 761
Jura M., 2003, ApJ, 584, L91
Jura M., 2008, AJ, 135, 1785
Jura M., Xu S., 2013, ApJ, 145, 30
Jura M., Young E. D., 2014, Annu. Rev. Earth Planet. Sci., 42, 45
Jura M., Farihi J., Zuckerman B., 2009, AJ, 137, 3191
Kalirai J. S., Hansen B. M. S., Kelson D. D., Reitzel D. B., Rich R. M., Richer H. B., 2008, ApJ, 676, 594
Kawka A., Vennes S., 2016, MNRAS, 458, 325
Kilic M., von Hippel T., Leggett S. K., Winget D. E., 2006, ApJ, 646, 474
Kleinman S. J. et al., 2013, ApJS, 204, 5
Koester D., Kepler S. O., 2015, A&A, 583, A86
Koester D., Wilken D., 2006, A&A, 453, 1051
Koester D., Rollenhagen K., Napiwotzki R., Voss B., Christlieb N., Homeier D., Reimers D., 2005, A&A, 432, 1025
Koester D., Gänsicke B. T., Farihi J., 2014, A&A, 566, A34
Manser C. J. et al., 2016, MNRAS, 455, 4467
Melis C., Jura M., Albert L., Klein B., Zuckerman B., 2010, ApJ, 722, 1078
Melis C. et al., 2012, ApJ, 751, L4
Metzger B. D., Rafikov R. R., Bochkarev K. V., 2012, MNRAS, 423, 505
Rafikov R. R., 2011, MNRAS, 416, L55
Rappaport S., Gary B. L., Kaye T., Vanderburg A., Croll B., Benni P., Foote J., 2016, MNRAS, in press
Rocchetto M., Farihi J., Gänsicke B. T., Bergfors C., 2015, MNRAS, 449, 574
Schlafly E. F., Finkbeiner D. P., 2011, ApJ, 737, 103
Smee S. A. et al., 2013, AJ, 146, 32
Tremblay P.-E., Bergeron P., Gianninas A., 2011, ApJ, 730, 128
Vanderburg A. et al., 2015, Nature, 526, 546
Vennes S., Kawka A., 2013, ApJ, 779, 70
Veras D., Gänsicke B. T., 2015, MNRAS, 447, 1049

Veras D., Leinhardt Z. M., Bonsor A., Gänsicke B. T., 2014, MNRAS, 445, 2244

Veras D., Leinhardt Z. M., Eggl S., Gänsicke B. T., 2015, MNRAS, 451, 3453

Vernet J. et al., 2011, A&A, 536, A105

Villaver E., Livio M., 2007, ApJ, 661, 1192

von Hippel T., Thompson S. E., 2007, ApJ, 661, 477

Voss B., Koester D., Napiwotzki R., Christlieb N., Reimers D., 2007, A&A, 470, 1079

Williams K. A., Bolte M., Koester D., 2009, ApJ, 693, 355

Wilson D. J., Gänsicke B. T., Koester D., Raddi R., Breedt E., Southworth J., Parsons S. G., 2014, MNRAS, 445, 1878

Wilson D. J., Gänsicke B. T., Koester D., Toloza O., Pala A. F., Breedt E., Parsons S. G., 2015, MNRAS, 451, 3237

Xu S., Jura M., 2014, ApJ, 792, L39

Xu S., Jura M., Klein B., Koester D., Zuckerman B., 2013, ApJ, 766, 132

Xu S., Jura M., Koester D., Klein B., Zuckerman B., 2014, ApJ, 783, 79

Xu S., Jura M., Dufour P., Zuckerman B., 2016, ApJ, 816, L22

Zuckerman B., Koester D., Reid I. N., Hünsch M., 2003, ApJ, 596, 477

Zuckerman B., Koester D., Melis C., Hansen B. M., Jura M., 2007, ApJ, 671, 872

Zuckerman B., Koester D., Dufour P., Melis C., Klein B., Jura M., 2011, ApJ, 739, 101

APPENDIX A: VELOCITIES AND VELOCITY GRADIENTS IN AN ECCENTRIC DISC

Horne & Marsh (1986) show that line photons travelling through an optically thick disc are more likely to escape along paths of the greatest velocity gradient. We derive and list here the equations needed to calculate the radial velocity and velocity gradient at any point in an elliptical disc of constant orbital eccentricity, e and constant orientation of its semi-major axes, a. This expands the formulation for modelling emission line profiles from circular discs described by Horne & Marsh (1986). We first set up the basic components of an eccentric orbit, of which some are shown in Fig. A1.

A1 Equations of an elliptical orbit

The polar equation for an ellipse is given as

$$r = \frac{l}{1 + e \cos \nu}, \tag{A1}$$

where l is the semi-latus rectum, and ν is the angle measured from the point of periastron, usually called the 'true anomaly'. Conservation of angular momentum in a central force field means that

$$r^2 \frac{d\nu}{dt} = h, \tag{A2}$$

where h, the specific angular momentum, is constant. This therefore leads to the true anomaly as a function of time being determined by the following equation

$$\frac{ht}{l^2} = \int_0^\nu \frac{d\nu'}{(1 + e \cos \nu')^2}. \tag{A3}$$

Making the substitution $z = \tan \nu/2$ and setting

$$z = \left(\frac{1+e}{1-e}\right)^{1/2} \tan \frac{E}{2}, \tag{A4}$$

where E is the eccentric anomaly (see Fig. A1), we get

$$E - e \sin E = \frac{h \left(1 - e^2\right)^{3/2}}{l^2} t. \tag{A5}$$

When $\nu = 2\pi$, we get $E = 2\pi$ and $t = P$, so then we can write

$$E - e \sin E = nt, \tag{A6}$$

where n is the mean angular velocity and is given by

$$n = \frac{2\pi}{P} = \frac{h \left(1 - e^2\right)^{3/2}}{l^2}. \tag{A7}$$

Equation (A6) is Kepler's equation of elliptical motion and can easily be solved numerically, and the true anomaly, ν, follows from

$$\tan \frac{\nu}{2} = \left(\frac{1+e}{1-e}\right)^{1/2} \tan \frac{E}{2}. \tag{A8}$$

E can be constructed geometrically by putting a circle radius a centred on the ellipse, and drawing a line perpendicular to the major axis through any point on the ellipse. The angle subtended by the point on the circle where the perpendicular line cuts it is E. Using this, or the above equation, one can show that

$$\cos E = \frac{e + \cos \nu}{1 + e \cos \nu}. \tag{A9}$$

Since E and ν always lie within the same range; 0 to π or π to 2π, this equation is sufficient to determine E. Related useful expressions are

$$\cos \nu = \frac{\cos E - e}{1 - e \cos E}, \tag{A10}$$

$$\sin \nu = \frac{\sqrt{1 - e^2} \sin E}{1 - e \cos E}. \tag{A11}$$

Assuming that the ellipse is oriented with the focus at the origin and the semi-major axis parallel to the x-axis (pointing left so that the periastron lies on the positive x-axis giving the standard orientation for ν in 2D polar coordinates, see Fig. A1), then the velocity at any point is given by

$$v_x = v_r \cos \nu - v_\nu \sin \nu, \tag{A12}$$

$$v_y = v_r \sin \nu + v_\nu \cos \nu, \tag{A13}$$

where

$$v_r = \frac{el \sin \nu}{(1 + e \cos \nu)^2} \dot{\nu}, \tag{A14}$$

and

$$v_\nu = \frac{l}{1 + e \cos \nu} \dot{\nu}, \tag{A15}$$

where

$$\dot{\nu} = \left(\frac{1+e}{1-e}\right)^{1/2} \left(\cos^2 \frac{E}{2} + \frac{1+e}{1-e} \sin^2 \frac{E}{2}\right)^{-1} \dot{E}, \tag{A16}$$

and

$$\dot{E} = \frac{n}{1 - e \cos E}. \tag{A17}$$

The equation for $\dot{\nu}$ can be reduced to

$$\dot{\nu} = \frac{\left(1 - e^2\right)^{1/2}}{(1 - e \cos E)^2} n, \tag{A18}$$

or, equivalently,

$$\dot{\nu} = \frac{(1 + e \cos \nu)^2}{\left(1 - e^2\right)^{3/2}} n, \tag{A19}$$
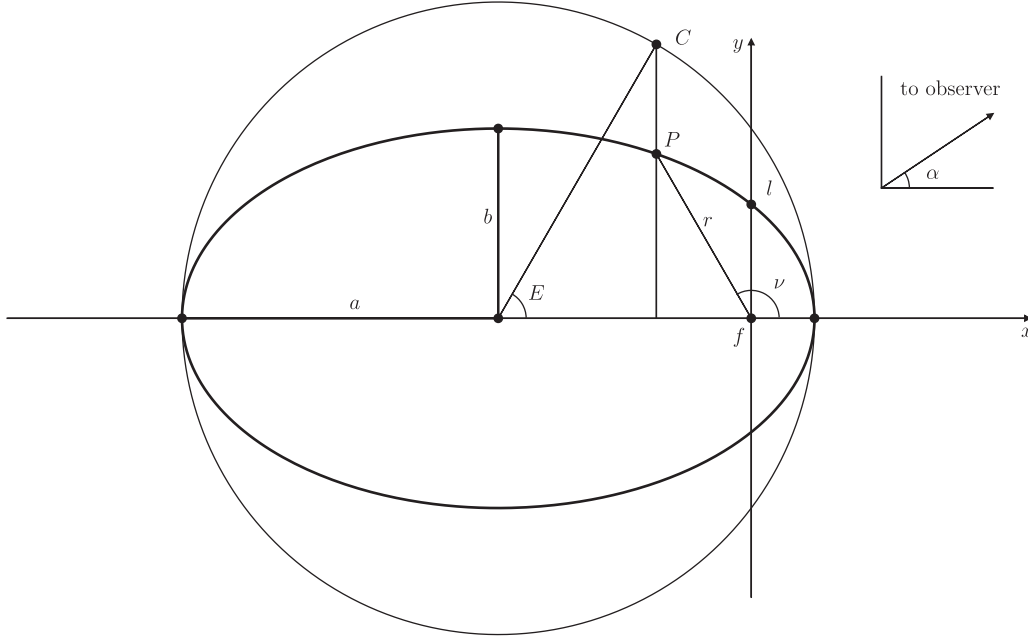
Figure A1. An elliptical orbit of eccentricity, e, with the origin centred on the focal point, f, with semi-major and semi-minor axes a and b. A point, P, along the orbit is shown, at a radius, r, and with a true anomaly, ν. The semi-latus rectum, l, is also labelled, as is the eccentric anomaly, E, which can be constructed geometrically by putting a circle of radius, a, centred on the ellipse, and drawing a line perpendicular to the major axis through any point (P, here) on the ellipse. The angle, α, to an observer is also shown, taken to be zero when the observer is looking along the x-axis from the positive side, and increases in the anti-clockwise direction.

giving the following alternative expressions for the two components of velocity (radial and azimuthal)

$$v_r = \frac{enl \sin \nu}{(1 - e^2)^{3/2}}, \tag{A20}$$

and

$$v_\nu = \frac{nl(1 + e \cos \nu)}{(1 - e^2)^{3/2}}. \tag{A21}$$

We are now in a position to consider orbits and radial velocities, and their derivatives.

A2 Velocity gradients in a confocal elliptical flow

If a point in the disc is viewed by an observer at angle α defined so that $\alpha = 0$ when looking along the positive x-axis and increasing anti-clockwise (see Appendix A), then its radial velocity is given by

$$v_r = v_x \cos \alpha + v_y \sin \alpha. \tag{A22}$$

Horne & Marsh (1986) showed that the velocity gradient is also required to fully model the emission profile of an accretion disc, which using the notation $v_{,x} \equiv \frac{\partial v}{\partial x}$, is given by

$$\frac{\mathrm{d}v_r}{\mathrm{d}k} = v_{r,x} \cos \alpha + v_{r,y} \sin \alpha, \tag{A23}$$

$$= v_{x,x} \cos^2 \alpha + \left(v_{x,y} + v_{y,x}\right) \cos \alpha \sin \alpha + v_{y,y} \sin^2 \alpha, \tag{A24}$$

where dk is a line element towards the observer. From equations (A12) and (A13), we have

$$v_{x,x} = v_{r,x} \cos \nu - v_{\nu,x} \sin \nu - (v_r \sin \nu + v_\nu \cos \nu)\nu_{,x}, \tag{A25}$$

$$v_{x,y} = v_{r,y} \cos \nu - v_{\nu,y} \sin \nu - (v_r \sin \nu + v_\nu \cos \nu)\nu_{,y}, \tag{A26}$$

$$v_{y,x} = v_{r,x} \sin \nu + v_{\nu,x} \cos \nu + (v_r \cos \nu - v_\nu \sin \nu)\nu_{,x}, \tag{A27}$$

$$v_{y,y} = v_{r,y} \sin \nu + v_{\nu,y} \cos \nu + (v_r \cos \nu - v_\nu \sin \nu)\nu_{,y}. \tag{A28}$$

One can show that

$$\nu_{,x} = -\frac{y}{r^2}, \tag{A29}$$

$$\nu_{,y} = \frac{x}{r^2}, \tag{A30}$$

while, using equations (A20) and (A21) we obtain,

$$v_{r,x} = e(1 - e^2)^{-3/2}[(n_{,x}l + nl_{,x}) \sin \nu + nl \cos(\nu)\nu_{,x}], \tag{A31}$$

$$v_{r,y} = e(1 - e^2)^{-3/2}[(n_{,y}l + nl_{,y}) \sin \nu + nl \cos(\nu)\nu_{,y}], \tag{A32}$$

$$v_{\nu,x} = (1 - e^2)^{-3/2}[(n_{,x}l + nl_{,x})(1 + e \cos \nu) - enl \sin(\nu)\nu_{,x}], \tag{A33}$$

$$v_{\nu,y} = (1 - e^2)^{-3/2}[(n_{,y}l + nl_{,y})(1 + e \cos \nu) - enl \sin(\nu)\nu_{,y}]. \tag{A34}$$

From equation (A1) we can obtain,

$$l_{,x} = r_{,x}(1 + e \cos \nu) - er \sin(\nu)\nu_{,x}, \tag{A35}$$

$$l_{,y} = r_{,y}(1 + e \cos \nu) - er \sin(\nu)\nu_{,y}, \tag{A36}$$

where

$$r_{,x} = \frac{x}{r}, \tag{A37}$$

$$r_{,y} = \frac{y}{r}, \tag{A38}$$

and from Kepler's third law, assuming the mass of the orbiting material to be negligible,

$$n^2 = \frac{GM}{a^3}, \tag{A39}$$

where G is the gravitational constant and M is the mass of the host star, we finally get the last unknowns,

$$n_{,x} = -\frac{3l_{,x}n}{2l}, \tag{A40}$$

$$n_{,y} = -\frac{3l_{,y}n}{2l}, \tag{A41}$$

which now allows one to calculate the velocity derivatives.

This paper has been typeset from a TeX/LaTeX file prepared by the author.